

Potentially Ferroelectric $\{Cu^{II}L_2\}_n$ Based Two-Dimensional Framework Exhibiting High Polarization and Guest-Assisted Dielectric Anomaly

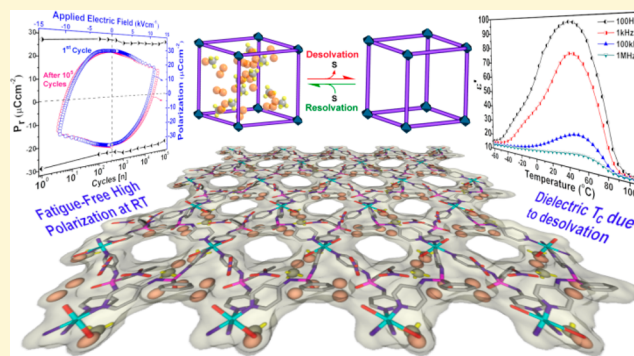
Anant Kumar Srivastava,[†] Pillutla Divya,[‡] B. Praveenkumar,^{*,‡} and Ramamoorthy Boomishankar^{*,†}

[†]Department of Chemistry, Indian Institute of Science Education and Research (IISER) Pune, Dr. Homi Bhabha Road, Pune, India 411008

[‡]PZT Centre, Armament Research and Development Establishment (ARDE), Defence Research and Development Organisation (DRDO), Dr. Homi Bhabha Road, Pune, India 411021

Supporting Information

ABSTRACT: Ferroelectrics in metal–organic materials have attracted recent interest owing to their synthetic simplicity and tunable nature. Utilizing isomeric dipodal phosphoramido ligands, L^1 [$PhPO(NH^3Py)_2$] and L^2 [$PhPO(NH^2Py)_2$], two new $Cu^{II}L_2$ derivatives, **1** ($\{[CuL_2(H_2O)_2] \cdot (NO_3)_2 \cdot (H_2O)_{1.5} \cdot (CH_3OH)\}_{\infty}$) and **2** ($[CuL_2] \cdot (NO_3)_2$), were synthesized. Compound **1** crystallizes in a noncentrosymmetric polar space group *Cc* as a two-dimensional framework, and **2** is a centrosymmetric complex. Electrical hysteresis (*P*–*E* loop) measurements on **1** at room temperature gave the remnant (P_r) and saturation (P_s) polarization values of 27.96 and 21.79 $\mu C \cdot cm^{-2}$, respectively, which are the highest among all of the known metal–organic ferroelectric materials. Also, the P_r value obtained for **1** is comparable to that of barium titanate and higher than most of the organic, polymeric, and inorganic ferroelectric materials. The permittivity measurements on **1** and **2** result in high dielectric constant values of 186.3 and 53.24, respectively, at 1 Hz frequency at room temperature. Temperature-dependent permittivity measurement on **1** yields a dielectric anomaly peak at 40 °C due to phase transition assisted by desolvation. The existence of phase transition is further confirmed by differential scanning calorimetry, powder X-ray diffraction, and polarized light microscopy. A comparison of the *P*–*E* loops of **1**, **1**_{desolvated}, and **1**_{resolvated} suggest that gasification/release of the solvate molecules from the packing structure affects the polarization in **1**.



INTRODUCTION

Materials having ferroelectric, multiferroic, and magnetoelectric properties are of tremendous research interest owing to their application in high-technique devices.^{1–7} Particularly ferroelectric materials, characterized by switchable electric polarization, are very attractive for their utility in nonvolatile computing devices, capacitors, micro-electromechanical systems (MEMS), semiconductor chips, field-effect transistors (FETs), telecommunication signal processing units, ultrasonic medical imaging devices, and nonlinear optical devices.^{8–21} Traditionally, ceramic materials of the perovskite family, for example barium titanate (BTO) and lead zirconate titanate (PZT), are used as commercial ferroelectrics.^{22–27} However, certain limitations such as high-temperature processing, higher molecular weight, and high content of toxic and expensive heavier metals, etc., triggered the search for alternate sources of ferroelectric materials.²⁸ In this effort, a range of new age materials, viz., polymers, organic–inorganic hybrids, small molecules, and liquid crystals, have been explored for ferroelectric and multiferroic applications.^{29–50} Currently, ferroelectric behavior in metal–organic materials has widely been examined due to their simple synthesis, flexibility, and low-temperature fabrication techniques.^{51,52} Moreover, the

structural components of the metal–organic assemblies, namely, metal ions, coordinating ligands, counteranions, and the guest molecules, provide a handle in imparting the required symmetry (polar point group) as well as tuning their ferroelectric behavior.^{53,54} Recently, starting from a flexible phosphoramido ligand, we have synthesized a family of anion-driven $[Cu^{II}L_2]_n$ coordination assemblies ($L = PhPO(NH^3Py)_2$; ³Py = 3-pyridyl) in discrete (centrosymmetric) and helical one-dimensional (1D) polymeric (noncentrosymmetric) structures. Interestingly, the presence of perchlorate or nitrate anions in the packing cavities of the 1D helical assemblies played a major role in tuning their ferroelectric behavior.⁵⁵ Inspired by these observations, we set out to explore the family of ferroelectric materials based on $[Cu^{II}L_2]_n$ assemblies by tuning various parameters. Specifically, we aimed at monitoring the change in structural topologies of $[Cu^{II}L_2]_n$ frameworks with subtle variations in the peripheral N-donor functionalities in phenyl phosphoric diamide backbone. Herein, we report the synthesis of two new assemblies, **1** ($\{[CuL_2(H_2O)_2] \cdot (NO_3)_2 \cdot (H_2O)_{1.5}$)

Received: April 6, 2015

Revised: July 15, 2015

Published: July 15, 2015

$(CH_3OH)\}_{\infty}$) and **2** ($[CuL^2_2 \cdot (NO_3)_2]$) based on the phosphoramido ligands $[PhPO(NH^4Py)_2]$ (L^1) and $[PhPO(NH^2Py)_2]$ (L^2), respectively. Compound **1** exhibits a non-centrosymmetric 2D polymeric structure, while **2** was obtained as a centrosymmetric discrete mononuclear complex. Ferroelectric measurements on **1** gave a high remnant polarization (P_r) value of $\sim 28 \mu C \cdot cm^{-2}$ at room temperature, which is the highest among all known metal–organic ferroelectric materials and is closely comparable with BTO. Temperature-dependent dielectric measurements on **1** show an interesting dielectric anomaly peak $\sim 40^\circ C$ due to desolvation indicating that the solvated molecules in the packing structure affect its overall polarization.

■ EXPERIMENTAL SECTION

General Remarks. All manipulations involving phosphorus halides were performed under dry nitrogen atmosphere in standard Schlenk glassware; toluene was dried over sodium. The 4-aminopyridine and 2-aminopyridine were purchased from Aldrich and used as received. PhPOCl₂ and Cu(NO₃)₂·3H₂O were purchased from Acros Organics and Merck, respectively, and used as received. NMR spectra were recorded on a JEOL 400 MHz spectrometer (¹H NMR, 400.13 MHz; ¹³C{¹H} NMR, 100.62 MHz; ³¹P{¹H} NMR, 161.97 MHz) at room temperature using SiMe₄ (¹H, ¹³C) and 85% H₃PO₄ (³¹P). The MALDI-TOF spectra were obtained on an Applied Biosystem MALDI-TOF/TOF spectrometer. The powder X-ray diffraction (PXRD) data were obtained from a Bruker-D8 Advance diffractometer. Thermal gravimetric analysis (TGA) data have been obtained from a PerkinElmer STA-6000 thermogravimetric analyzer. Polarized light microscope images of the crystals were recorded by using a LEICA DM2500P microscope equipped with a Linkam TMS 94 heating stage. Elemental analyses were performed on a Vario-EL cube elemental analyzer. FT-IR spectra were taken on a PerkinElmer spectrophotometer with samples prepared as KBr pellets. FT-IR in attenuated total reflectance (ATR) mode was taken on neat samples on a Bruker Alpha spectrophotometer. Melting points were obtained using an Electrothermal melting point apparatus and were uncorrected.

Synthesis. Ligand L¹. To a well-stirred suspension of 4-aminopyridine (11.756 g, 125 mmol) in chloroform (~ 200 mL) at $0^\circ C$, PhPOCl₂ (2.5 mL, 3.475 g, 17.82 mmol) in 10 mL of chloroform was added dropwise. The reaction mixture was refluxed for 6 h, and the obtained residue was filtered and washed 3 times with water. This was then dried in a vacuum desiccator and collected. Rod-like colorless crystals suitable for single crystal X-ray diffraction (SCXRD) analysis were obtained from its MeCN solution after 4–5 days. Yield: 4.66 g (84%). Mp: 195–200 °C. ¹H NMR (400 MHz, (CD₃)₂SO): δ 3.28 (m, 2H, NH), 7.14 (d, 4H, CH(pyridyl)), 7.61 (m, 3H, CH(phenyl)), 7.91 (m, 2H, CH(phenyl)), 8.01 (s, 2H, CH), 8.2 (d, 4H, CH(pyridyl)). ¹³C NMR (100 MHz, (CD₃)₂SO): δ 112.97, 129.18, 132.08, 133.11, 149.48, 150.59. ³¹P NMR (162 MHz, {(CD₃)₂SO}): δ 11.79. FT-IR data in KBr pellet (cm⁻¹): 3485, 1611, 1571, 1506, 1467, 1409, 1332, 1274, 1180, 1120, 1067, 926, 827, 756, 689, 661, and 520. ESI-MS: 311 (M + H)⁺. Anal. Calcd for C₁₆H₁₅N₄OP: C, 61.93; H, 4.87; N, 18.06. Found: C, 61.75; H, 4.91; N, 17.99.

Ligand L². To a stirred solution of 2-aminopyridine (11.756 g, 125 mmol) in toluene (~ 200 mL) at $0^\circ C$, PhPOCl₂ (2.5 mL, 3.475 g, 17.82 mmol) in 10 mL of toluene was added dropwise. The reaction mixture was refluxed for 4 h, and the

obtained residue was filtered and washed 3–4 times with water. This was then dried in a vacuum desiccator and collected. Regular shaped colorless crystals suitable for SCXRD analysis were obtained from its solution in MeOH/MeCN after 2–3 days. Yield: 5.08 g (92%). Mp: 220 °C. ¹H NMR (400 MHz, (CD₃)₂SO): δ 6.86 (t, 2H, CH(pyridyl)), 7.06 (d, 2H, CH(pyridyl)), 7.48 (m, 2H, CH(phenyl)), 7.54 (d, 1H, CH(phenyl)), 7.59 (t, 2H, CH(phenyl)), 7.91 (dd, 2H, CH(pyridyl)), 8.12 (d, 2H, CH(pyridyl)), 8.67 (s, 2H, NH). ¹³C NMR (100 MHz, (CD₃)₂SO): δ 111.77, 116.80, 128.71, 132.06, 134.40, 138.32, 148.13, 155.08. ³¹P NMR (162 MHz, {(CD₃)₂SO}): δ 8.62. FT-IR data in KBr pellet (cm⁻¹): 3467, 1589, 1481, 1379, 1201, 1129, 1057, 939, 824, 721, 685, 659, 514. ESI-MS: 311 (M + H)⁺. Anal. Calcd for C₁₆H₁₅N₄OP: C, 61.93; H, 4.87; N, 18.06. Found: C, 62.03; H, 4.87; N, 17.87.

Compound 1. To a stirred and filtered solution of L¹ (62 mg, 0.2 mmol) in MeOH (3 mL), water (3 mL) was layered carefully, followed by a careful layer of solution of Cu(NO₃)₂·6H₂O (24.5 mg, 0.1 mmol) in MeOH (3 mL). The resultant mixture was then kept undisturbed at room temperature (RT) in a screw-capped vial. Blue crystals of **1** suitable for SCXRD analysis were recovered after 4–5 weeks. Yield: 41% (37 mg), based on Cu. FT-IR data in KBr pellet (cm⁻¹): 3488, 1615, 1577, 1509, 1384, 1333, 1293, 1214, 1124, 1066, 1024, 933, 838, 756, 694, 662, 521. Anal. Calcd for C₃₃H₄₁N₁₀O_{12.5}P₂Cu: C, 43.88; H, 4.58; N, 15.51. Found: C, 43.75; H, 4.71; N, 15.52.

Compound 2. To a gently heated stirred solution of L² (62 mg, 0.2 mmol) in MeOH (3 mL) and MeCN (2 mL), Cu(NO₃)₂·6H₂O (24.1 mg, 0.1 mmol) in MeOH (5 mL) was added. The blue solution was then filtered through a thick pad of Celite and left for crystallization at RT. Blue crystals of **2** suitable for SCXRD analysis were obtained within 2–3 weeks. Yield: 52% (21 mg), based on Cu. FT-IR data in KBr pellet (cm⁻¹): 1607, 1581, 1507, 1468, 1383, 1270, 1193, 1125, 1061, 1025, 945, 805, 691, 621, 519, 501. Anal. Calcd For C₃₂H₃₀CuN₁₀O₈P₂: C, 47.56; H, 3.74; N, 17.33. Found: C, 47.49; H, 3.69; N, 17.27.

Compound 1_{desolvated}. This was obtained by heating **1** at 60 °C under vacuum for 12 h. The formation of the desolvated phase of **1** was confirmed by PXRD and TGA analysis.

Compound 1_{resolvated}. This was obtained by the exposure of **1_{desolvated}** to the mixture of MeOH and water vapors inside a screw-capped vial. Rapid formation of **1_{resolvated}** can be observed upon adding a few drops of the mother liquor of **1** to a sample of **1_{desolvated}**.

Crystallography. Reflections were collected on a Bruker Smart Apex Duo diffractometer at 100 K using Mo K α radiation ($\lambda = 0.71073 \text{ \AA}$) for L¹, L², **1_sq**, and **2**. Structures were refined by full-matrix least-squares against F² using all data (SHELX).⁵⁶ Crystallographic data for all of these compounds are listed in Tables S1–S6 (Supporting Information). All non-hydrogen atoms were refined anisotropically if not stated otherwise. Hydrogen atoms were constrained in geometric positions to their parent atoms. Crystals of L¹ were weakly diffracting at higher angles, and hence a $2\theta = 50^\circ$ cutoff was applied. Two nitrate anions and two phenyl rings in **1** were thermally disordered. Atom positions of the disordered groups were freely refined isotropically over two positions using similar distances and similar U-restraints. The solvate methanol and water molecules in **1** were disordered and, hence, were treated as diffuse contributions to the overall scattering and removed by the SQUEEZE/PLATON for a better refinement data (in

the case of **1_sq**). The exact amount of the solvate water molecules was further confirmed by TGA data. The refinement parameter in **1** was slightly higher owing to the diffuse nature of the solvated crystals. Unit cell parameters for **1** at 40 °C were obtained on a Bruker D8 Venture diffractometer with Microfocus X-ray source and photon detector after heating the single crystal under hot N₂ flow for 24 h. However, the weak reflections were not sufficient enough to yield an acceptable structure.

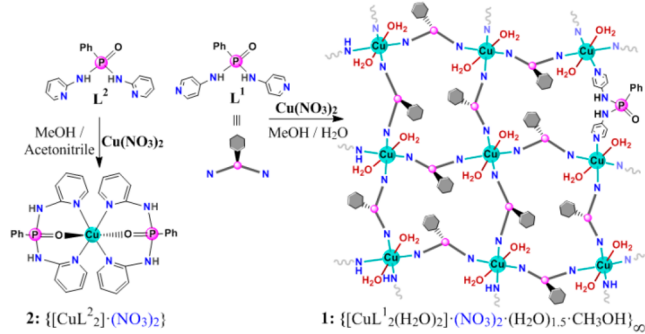
Ferroelectric and Dielectric Measurements. In order to determine the dielectric and ferroelectric properties, the powdered samples of **1** and **2** were compacted in the form of discs (of approximately 10 mm diameter and 1 mm thickness). The compacted discs were subsequently electrodeed using aluminum adhesive foils for both ferroelectric and dielectric measurements. The dielectric characteristics for **1** and **2** were measured using the Novocontrol dielectric spectrometer.

The ferroelectric hysteresis loops in **1** were measured by using a Sawyer–Tower circuit. The measurements pertaining to polarization and fatigue cycles were recorded using a hysteresis loop analyzer (TF Analyzer 2000, aixACCT, Aachen, Germany). Leakage current was measured dynamically for various voltage steps during the hysteresis loop measurements.

■ RESULTS AND DISCUSSION

Syntheses and Crystal Structures. The phosphoric diamide ligands L¹ and L² were synthesized by reacting PhPOCl₂ with 4- and 2-aminopyridine, respectively. Ligands L¹ and L² were characterized by mass spectra, ¹H, ¹³C, and ³¹P NMR spectroscopy, and single crystal X-ray diffraction techniques (Figures S1–S10, Supporting Information). The 2D coordination polymer **1** was isolated as blue colored crystals in a 2:1 reaction mixture involving L¹ and Cu(NO₃)₂ in MeOH/H₂O medium at room temperature. The mononuclear complex **2** was prepared in a similar 2:1 reaction of L² with Cu(NO₃)₂ in MeOH/MeCN medium at room temperature (Scheme 1).

Scheme 1. Formation of **1 and **2****



The crystal structure of **1** was solved in the monoclinic noncentric polar space group Cc, point group “m”, and point group symmetry “C_s” (Tables S1–S6, Supporting Information). The asymmetric unit consists of a Cu(II) ion, two ligand motifs, two charge-balancing (noncoordinating) nitrate ions disordered over four positions, two coordinated water molecules, and solvated molecules of methanol and water (Figure S11, Supporting Information). The molecular structure of **1** consists of a cationic 2D polymeric structure of composition $\{[\text{Cu}^{II}\text{L}_1^2(\text{H}_2\text{O})_2]^{2+}\}_n$ (Figure 1a). The Cu(II)

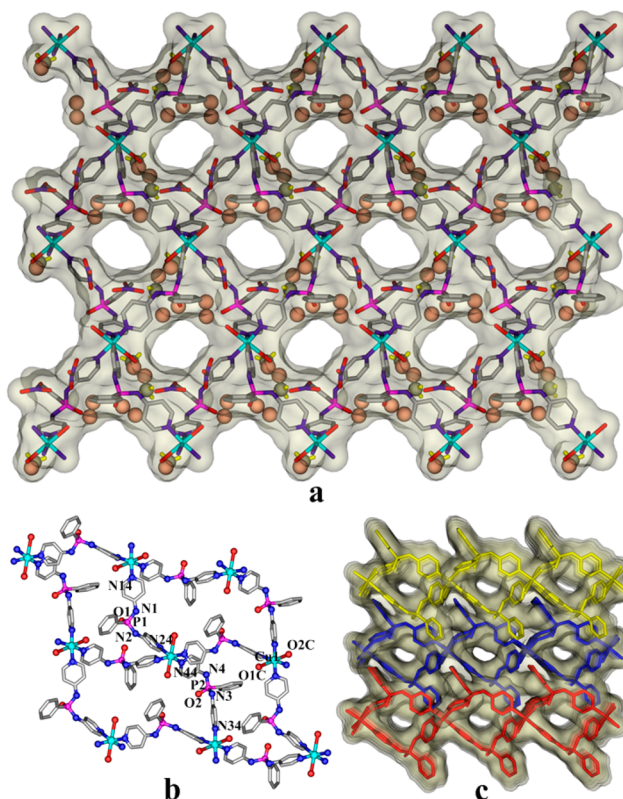


Figure 1. (a) View of the 2D framework in **1**. The “C” and “O” atoms of the solvate molecules are depicted as gray and beige colored spheres, respectively and “H” atoms as yellow straws. (b) Segment of the 2D assembly showing the crisscross orientation of the adjoined macrocycles. (c) Packing diagram of the cationic assembly in **1** along the *b*-axis showing the presence of intrinsic and extrinsic cavities. The individual 2D layers are colored differently for clarity.

ions are located in a distorted octahedral environment with four N_{pyridyl} contacts from four different ligand units and two coordinated water molecules. Each ligand motif acts as a bridge between two Cu(II) centers and is part of two 48-membered Cu₄L₄ macrocycles. Thus, the cationic $[\text{Cu}^{II}\text{L}_1]_n$ network in **1** consists of a contiguous array of Cu₄L₄ edge-shared macrocycles in which the Cu(II) ions act as the corner atoms (Figure 1b). Two unique Cu···Cu distances have been found within each macrocycle, 12.107 and 11.617 Å, owing to two crystallographically unique ligand scaffolds. The diagonal Cu···Cu distances in these macrocycles vary by a large margin with the longer one having a distance of 20.323 Å and the shorter one being at 12.212 Å. The interlayer distance in **1** is in the range between 8.515 and 9.049 Å (Figure S12, Supporting Information). TOPOS analysis^{57,58} for **1** gave a four-connected uninodal sqI/Shubnikov tetragonal plane net represented by the Schläfli symbol {4⁴.6²} (Supporting Information).^{59,60} The packing diagram of **1** shows the presence of both intrinsic and extrinsic cavities which are filled with nitrate anions and solvate molecules (Figure 1c). While the extrinsic cavity partially contains the solvated methanol, the intrinsic cavity contains the solvated water, part of methanol and nitrate anions. However, all of the solvated molecules and anions form H-bonded 1D wires which interact with the host framework through the coordinated water molecules (Figures S13 and S14, Supporting Information). The TGA trace of **1** infers a 10% weight loss in the temperature range between 40 and 100 °C, which corresponds to the loss of 3.5 molecules of water (both

coordinated and solvated) and a molecule of methanol (Figure S15, *Supporting Information*).

The crystal structure of **2** was solved as a mononuclear complex in the tetragonal centrosymmetric space group $I4_1/a$ (point group “ $4/m$ ” and point group symmetry “ C_{4h} ”). The asymmetric unit of **2** contains a Cu(II) ion with half-occupancy, one phosphoramido ligand and a nitrate anion for charge balance. The Cu(II) ion is located in an octahedral coordination with four N_{pyridyl} and two O_{phosphoryl} contacts in which each L² moiety acts as a cis-directed N,N,O-coordinating ligand (Figures S16 and 17, *Supporting Information*).

Ferroelectric and Dielectric Studies. An important characteristic of ferroelectric materials is the observation of a ferroelectric hysteresis loop. Hence the ferroelectric measurements were performed on the sample of **1**, as it is noncentrosymmetric and belongs to one of the 10 polar point groups (1, *m*, 2, *mm*2, 3, 3*m*, 4, 4*mm*, 6, and 6*mm*) essential for the ferroelectric behavior.^{61,62} The measurements show a well-defined rectangular polarization (*P*) vs electric field (*E*) loop at 0.1 and 1 Hz frequencies. Remarkably high remnant polarization (*P_r*) values of 27.95 (0.1 Hz) and 28.53 (1 Hz) $\mu\text{C}\cdot\text{cm}^{-2}$ are obtained for **1**. The saturation polarization (*P_s*) values for the *P*-*E* loops are found to be 21.79 (0.1 Hz) and 18.35 (1 Hz) $\mu\text{C}\cdot\text{cm}^{-2}$; the coercive fields obtained in these measurements (*E_c*) are 5.9 and 9.7 $\text{kV}\cdot\text{cm}^{-1}$ at 0.1 and 1 Hz frequencies, respectively (Figure 2 and Figure S19, *Supporting Information*). The leakage current densities are in the range between 10^{-4} and $10^{-8} \text{ A}\cdot\text{cm}^{-2}$, indicating that the observed hysteresis loops are clearly due to ferroelectricity. To the best of our knowledge, the polarization value obtained for **1** is the highest among all of the ferroelectric metal–organic self-assemblies known so far, higher than several organic, molecular, and polymeric ferroelectric materials, and is closely comparable with BTO (26 $\mu\text{C}\cdot\text{cm}^{-2}$).^{33,34} Also, it is significantly higher in comparison with KDP and NaNO₂ and the previously reported 1D helical $[\text{Cu}^{\text{II}}\text{L}_2]_n$ assembly (Table S7, *Supporting Information*).

The retention of ferroelectric polarization for **1** was probed by fatigue studies (loss of remnant polarization during bipolar switching cycles) at 1 Hz frequency. From Figure 2b it is clearly evident that the *P_r* value and the rectangular shape of the hysteresis loop is completely retained after 10^5 switching cycles. This is attributed to a facile reversal of domain switching and absence of accumulation of space charge that pins the domain walls,⁶³ confirming the fatigue-free ferroelectric behavior in **1**. The fatigue resistance of **1** may be attributed to its dense charge-separated metal–organic framework (MOF) structure, along with guest solvents, which provides a steady polarization even for higher switching cycles. The PXRD data obtained on the compacted disc, both before and after measurements, remained unchanged and matched with that of the as-synthesized **1**, confirming the stability of the framework during disc formation as well as *P*-*E* loop measurements (Figure S20, *Supporting Information*).

It is interesting to note that the ferroelectric polarization value in **1** is significantly higher than the previously reported 1D helical $[\text{Cu}^{\text{II}}\text{L}_2]_n$ based assembly. While the 1D helical assembly was crystallized in the higher symmetric trigonal space group (R_3 , point group C_3),⁵⁵ compound **1** is obtained in the lower symmetric monoclinic space group (Cc , point group C_s). In addition, the packing diagram of the 1D helical assembly contains only the extrinsic channels, occupied by the perchlorate anions and solvate molecules (methanol and

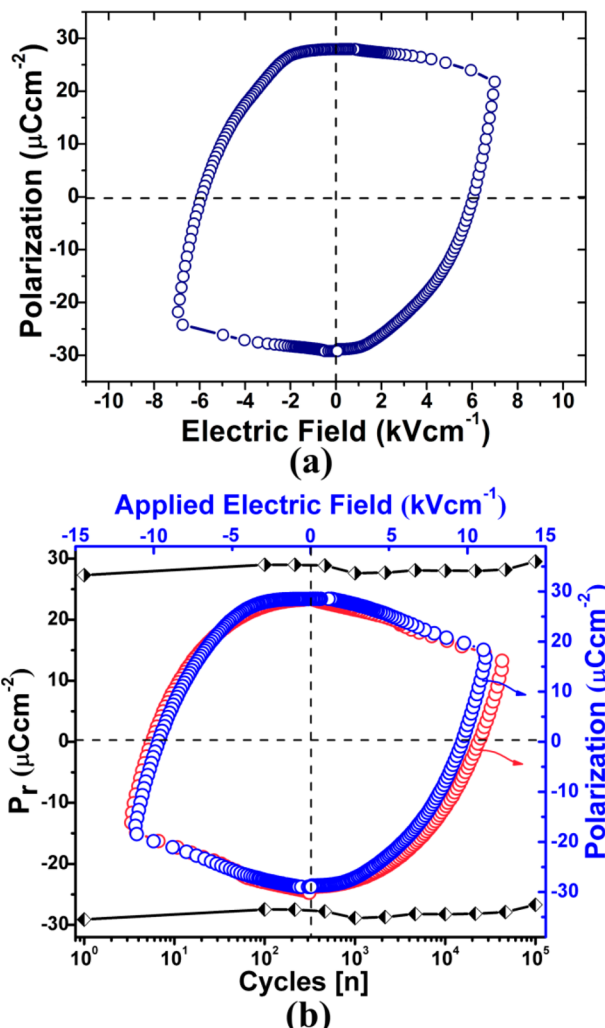


Figure 2. Dielectric hysteresis measurement of **1**: (a) *P*-*E* loop at 0.1 Hz. (b) Ferroelectric fatigue studies and *P*-*E* loop before (blue) and after (pink) fatigue measurements at 1 Hz.

water) that interact with the host framework and not among themselves (Figure S18, *Supporting Information*),⁵⁵ whereas, in **1**, the anions and the polar solvent molecules form H-bonded wire-like structures which are located at the intrinsic channels present within the 2D sheet (Figures S13 and S14, *Supporting Information*). These H-bonded wires further interact with the coordinated water molecules positioned along the walls of the cavities and ensure an effective long-range interaction between the ionic pairs. Although it is difficult to predict the precise origin of ferroelectricity in **1** and in metal–organic materials in general (owing to their complex structure), the spatial asymmetry (polar point group) and ordered arrangement of polar solvent, in the form of wire or cluster restricted in a confined environment such as carbon nanotube, nanopore membranes, and porous MOFs, have been shown to induce ferroelectric polarization.^{64–66} Thus, the H-bonded wires of polar solvents and anions in a confined region of lower symmetry could be the reason for the enhanced polarization in **1** in comparison with the previously reported 1D helical $[\text{Cu}^{\text{II}}\text{L}_2]_n$ based assembly.

The frequency-dependent dielectric permittivity (ϵ) studies were performed on **1** with varying temperatures (30–100 °C). Figure 3a depicts a plot of the real part of dielectric permittivity

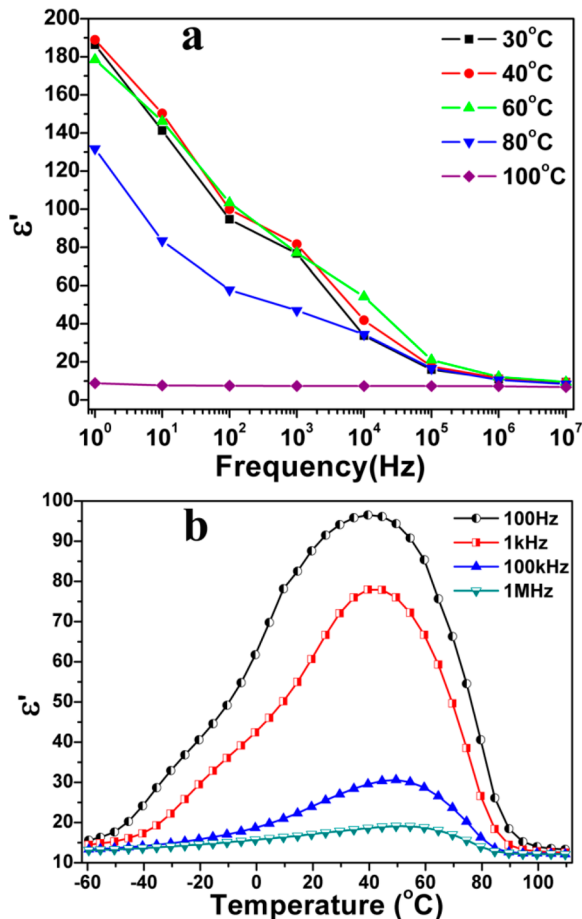


Figure 3. (a) Frequency dependence of the real part of the dielectric constant of **1** at different temperatures. (b) Temperature dependence of the dielectric constants measured at various frequencies showing the presence of T_c around 40 °C.

(ϵ') as a function of frequency showing a maximum ϵ' value of 188.9 at 40 °C at 1 Hz frequency. The observed ϵ' values at room temperature (30 °C) are found to be 186.3 and 94.7 at 1 and 100 Hz frequencies, respectively. The high room temperature dielectric permittivity value of **1** also supports its ferroelectric nature. Permittivity measurements on **2** (Figures S21 and S22, Supporting Information) show a reasonable ϵ' value of 53.24 at 30 °C in 1 Hz frequency. The observed decrease in ϵ' with increase in frequency is attributed to the contribution of all polarization mechanisms at lower frequencies.⁵⁵ Furthermore, the temperature dependence of the dielectric constant of **1** was measured at various frequencies between 10^2 and 10^6 Hz (Figure 3b). An initial increase in the ϵ' values of **1** with an increase in temperature is found starting from -60 °C up to 40 °C. Beyond this point a gradual decrease in ϵ' values is observed. As a result, an anomalous dielectric peak is observed with $T_c = 40$ °C with a maximum ϵ' value of 96.5 at 100 Hz indicating the presence of phase transition due to desolvation. This may be attributed to the break in long-range interaction within the structural components of **1** during desolvation. The anomaly peak gradually decreases in intensity with marginal shift in the dielectric maxima to higher temperatures upon increasing the frequency of measurement. This can be attributed to the dielectric relaxation phenomenon assisted by desolvation.⁵³ However, the measured dielectric loss factors in both **1** and **2** are invariably low suggesting them as a

good dielectric material for practical utility (Figures S21–S26, Supporting Information).⁶⁷

The existence of desolvation-assisted T_c in **1** is also evident from the differential scanning calorimetry (DSC) analysis which displays an endothermic peak at around 55 °C associated with an irreversible phase transition (Figure S27, Supporting Information).⁶⁸ The variable temperature powder X-ray diffraction (PXRD) analysis also exhibits a change in peak patterns above 40 °C (Figure 4a and Figure S28, Supporting Information). The PXRD obtained in the temperature range between 50 and 270 °C remained almost the same and matched very well with the desolvated sample of **1**. The single crystal X-ray diffraction patterns of **1** at various temperatures between -173 and 40 °C (on a Bruker Smart Apex Duo diffractometer) indicates the weakening of the diffraction spots at higher temperatures (Figure S29, Supporting Information). Performing the data collection on a Bruker D8 Venture diffractometer with Microfocus X-ray source gave satisfactory unit cell parameters for **1** at 40 °C. A change in cell parameters along all three axes was observed at 40 °C (Figures 4c and S30, Supporting Information). These unit cell parameters agree well with those extracted from indexing the PXRD of **1**_{desolvated} (Table S8, Supporting Information). This suggests changes in both in-plane structure and interlayer distances with no abrupt changes in the parent metal–ligand assembly in **1** during desolvation. The FT-IR spectra in ATR mode for the neat samples of **1**, **1**_{desolvated}, and **1**_{resolvated} gave almost identical peak patterns except for **1**_{desolvated} where the -OH (water and methanol) stretching frequency peaks were absent (Figure S31, Supporting Information). The polarized light microscope (PLM) images in the temperature range between 30 and 100 °C show that the transparent crystals **1** turned opaque above 40 °C during the desolvation process (Figure 4d–g). However, the original state of the crystals has been recovered upon addition of a few drops of the mother liquor (Figure 4h). In fact, the broadened nature of the anomalous dielectric peak (associated with T_c) can be related to the change in polarizability of **1** due to gasification or release of solvated molecules of water and methanol at that temperature (Figure 4b,c).

In order to study the role of solvated molecules on the ferroelectric behavior of **1**, the ferroelectric hysteresis measurements were performed on desolvated and resolvated samples of **1**. The P – E loop of **1**_{desolvated} shows the behavior of a resistor-like material.⁶⁹ However, **1**_{resolvated} gave a P – E loop as well as polarization values similar to that of as-made **1** (Figure 5a). In a related report, Mak and co-workers observed a reversible switching of ferroelectric and paraelectric states in a 3D framework induced by solvate molecules.⁶⁶ The leakage current density of **1**_{resolvated} (10^{-4} – 10^{-8} A·cm⁻²) measured as a function of voltage also shows a close resemblance to that of **1**, while **1**_{desolvated} shows a much lower leakage current density of 10^{-7} – 10^{-10} A·cm⁻² (Figure 5b). Thus, the increased leakage current density for **1**, vis-à-vis **1**_{resolvated}, in comparison with that of **1**_{desolvated} illustrates the extrinsic effects caused by solvate molecules toward the polarization.⁷⁰ This implies that resolvation restores the long-range interaction between the ionic pairs (cationic and anionic components of the framework) that are responsible for the polarization. In addition, there is no significant change in leakage current of all the samples when the voltage polarity is reversed. Subsequently, in the intermediate electric field region a space–charge limited current conduction behavior is observed. This is due to the electric charge, in dielectrics, being considered as a continuum of charge

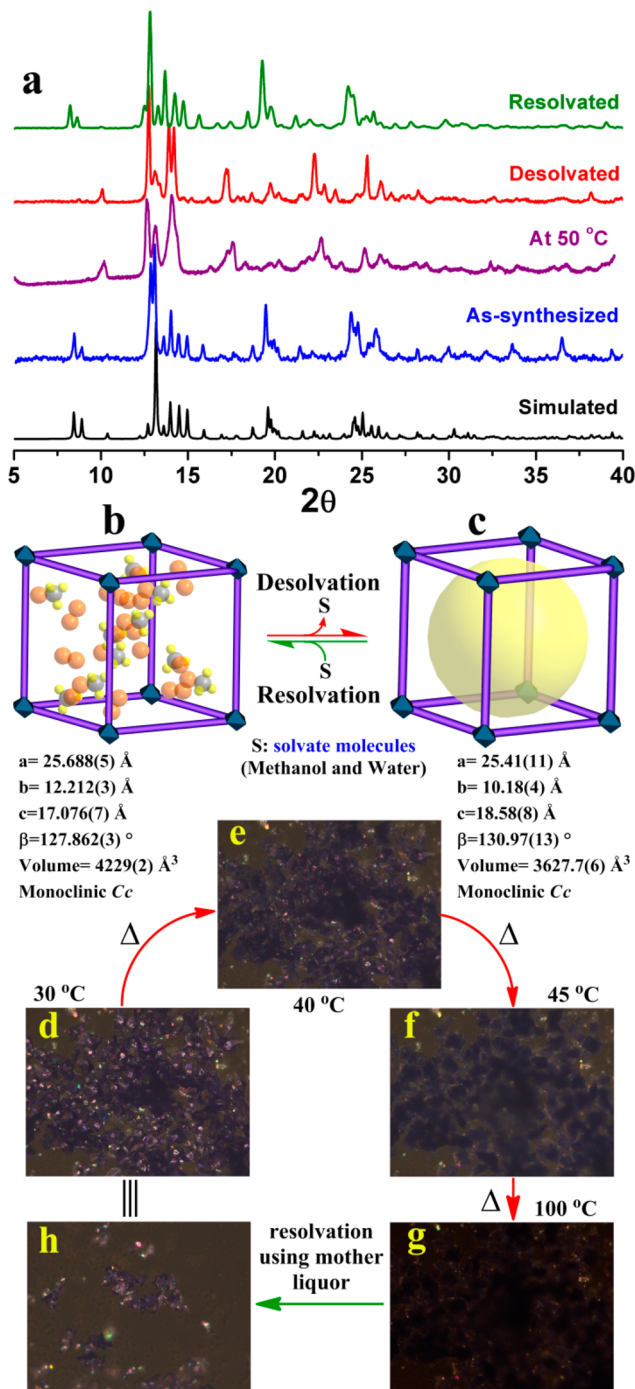


Figure 4. (a) Powder X-ray diffraction (PXRD) profiles of various samples of **1**. (b) Unit cell box of **1** showing the location of solvate molecules. The cationic $[\text{Cu}^{\text{II}}\text{L}_2]_n$ framework and nitrate anions have been removed for clarity. (c) Unit cell box obtained from the 40 °C data indicating the structural changes due to desolvation. Hot-stage PLM images of crystals of **1** during desolvation (d–g) and resolvation (h).

distributed over a region of space.⁷¹ It is noteworthy to mention that such a type of solvent-assisted dielectric transition and high ferroelectric polarization may not originate solely from the 1D arrangement of the polar solvents, H_2O and MeOH.^{72–74} Nevertheless, in **1** the polarization is due to the collective contributions from the H-bonded chain-like arrangement of the solvate molecules and nitrate anions and their

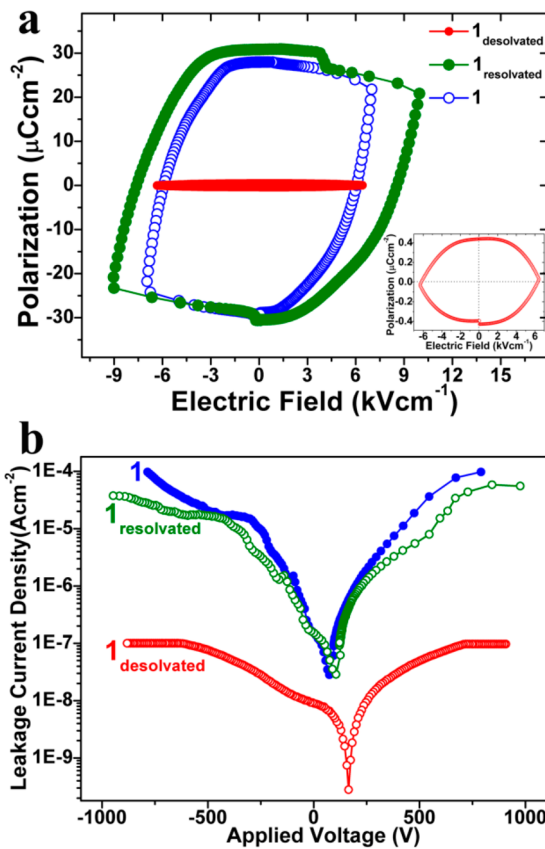


Figure 5. (a) Dielectric hysteresis loops of the as-synthesized, desolvated, and resolvated samples of **1**. Inset: closer view of the P – E loop of **1**_{desolved} showing a resistor-type behavior. (b) Plots of leakage current density as a function of applied voltage for the as-synthesized, desolvated, and resolvated samples of **1**.

cumulative interactions with the cationic $\{[\text{Cu}^{\text{I}}\text{L}_2(\text{H}_2\text{O})_2]^{2+}\}_n$ host framework.

CONCLUSION

The present study demonstrates the tunable nature of ferroelectric behavior in metal–ligand assemblies, such as $[\text{Cu}^{\text{II}}\text{L}_2]_n$ frameworks, via ligand-driven dimensionality control. The cationic two-dimensional $[\text{Cu}^{\text{II}}\text{L}_2]_n$ framework **1** shows a very high remnant polarization, P_r , which is the highest among all of the reported metal–organic ferroelectric materials. While there is a 10-fold increase in the P_r value of **1** in comparison with the previously reported $[\text{Cu}^{\text{II}}\text{L}_2]_n$ based 1D helical framework, the monomeric $[\text{Cu}^{\text{II}}\text{L}_2]$ assembly of **2** is centrosymmetric and exhibits no ferroelectric behavior. However, both **1** and **2** show high dielectric permittivity values. A T_c value of 40 °C was obtained in the temperature-dependent permittivity measurements for **1**, attributed to the loss of solvate molecules. The P – E measurements done on the desolvated and resolvated samples of **1** indicate that the solvated molecules in the packing structure of **1** affect the polarization of the framework. Currently, we are focused on developing new synthetic strategies for obtaining a family of metal–organic materials with tunable dielectric, ferroelectric, and multiferroic properties.

■ ASSOCIATED CONTENT

● Supporting Information

X-ray crystallographic data for L¹, L², 1, 1_sq, and 2 in the CIF format, figures showing NMR and mass spectra for L¹ and L², crystal structures and dielectric measurements, and PXRD, TGA, and TOPOS analyses, conductivity vs frequency plots, diffraction spots, FT-IR spectra, and tables listing crystallographic data collection, bond lengths, bond angles, hydrogen bonding, saturation polarization and coercive field values, and unit cell parameter comparison. The Supporting Information is available free of charge on the ACS Publications website at DOI: 10.1021/acs.chemmater.5b01267.

■ AUTHOR INFORMATION

Corresponding Authors

*E-mail: boomi@iiserpune.ac.in (R.B.).

*E-mail: praveenkumar@arde.drdo.in (B.P.).

Notes

The authors declare no competing financial interest.

■ ACKNOWLEDGMENTS

This work was supported by IISER, Pune and the Department of Science and Technology, India through Grant No. SR/S1/IC-50/2012 (R.B.). The DST-FIST Level 2 Grant is acknowledged for procuring the Bruker D8 Venture Diffractometer with Microfocus X-ray source at IISER, Pune. We thank Dr. R. Vaidhyanathan for help with PXRD analysis.

■ REFERENCES

- (1) Cheetham, A. K.; Rao, C. N. R. There's Room in the Middle. *Science* **2007**, *318*, 58–59.
- (2) Whatmore, R. Ferroelectric Materials. *Springer Handbook of Electronic and Photonic Materials*; Springer: New York, 2007; pp 597–623.
- (3) Cheong, S.-W.; Mostovoy, M. Multiferroics: a magnetic twist for ferroelectricity. *Nat. Mater.* **2007**, *6*, 13–20.
- (4) Ramesh, R. Materials science: Emerging routes to multiferroics. *Nature* **2009**, *461*, 1218–1219.
- (5) Ramesh, R.; Spaldin, N. A. Multiferroics: progress and prospects in thin films. *Nat. Mater.* **2007**, *6*, 21–29.
- (6) Eerenstein, W.; Mathur, N. D.; Scott, J. F. Multiferroic and magnetoelectric materials. *Nature* **2006**, *442*, 759–765.
- (7) Spaldin, N. A.; Fiebig, M. The renaissance of magnetoelectric multiferroics. *Science* **2005**, *309*, 391–392.
- (8) Das, S.; Appenzeller, J. FETRAM. An organic ferroelectric material based novel random access memory cell. *Nano Lett.* **2011**, *11*, 4003–4007.
- (9) Dawber, M.; Rabe, K. M.; Scott, J. F. Physics of thin-film ferroelectric oxides. *Rev. Mod. Phys.* **2005**, *77*, 1083–1130.
- (10) De Araujo, C. A.-P.; Cuchiaro, J. D.; McMillan, L. D.; Scott, M. C.; Scott, J. F. Fatigue-free ferroelectric capacitors with platinum electrodes. *Nature* **1995**, *374*, 627–629.
- (11) Han, S.-T.; Zhou, Y.; Roy, V. A. L. Towards the Development of Flexible Non-Volatile Memories. *Adv. Mater.* **2013**, *25*, 5425–5449.
- (12) Lee, H. N.; Christen, H. M.; Chisholm, M. F.; Rouleau, C. M.; Lowndes, D. H. Strong polarization enhancement in asymmetric three-component ferroelectric superlattices. *Nature* **2005**, *433*, 395–399.
- (13) Rijnders, G.; Blank, D. H. A. Materials science: Build your own superlattice. *Nature* **2005**, *433*, 369–370.
- (14) Salje, E. K. H.; Scott, J. F. Ferroelectric Bloch-line switching: A paradigm for memory devices? *Appl. Phys. Lett.* **2014**, *105*, 252904.
- (15) Scott, J. F. Applications of modern ferroelectrics. *Science* **2007**, *315*, 954–959.
- (16) Scott, J. F.; Paz de Araujo, C. A. P. Ferroelectric memories. *Science* **1989**, *246*, 1400–1405.
- (17) Vanderah, T. A. Talking ceramics. *Science* **2002**, *298*, 1182–1184.
- (18) Lines, M. E.; Glass, A. M. *Principles and applications of ferroelectrics and related materials*. Clarendon Press: Oxford, U.K., 1977.
- (19) Scott, J. F. *Ferroelectric memories*; Springer Science & Business Media: Heidelberg, Germany, 2000; Vol. 3.
- (20) Uchino, K. *Ferroelectric Devices*, 2nd ed.; CRC Press: Boca Raton, FL, USA, 2009.
- (21) Xu, Y. *Ferroelectric materials and their applications*. Elsevier: Amsterdam, 2013.
- (22) Haertling, G. H. Ferroelectric ceramics: history and technology. *J. Am. Ceram. Soc.* **1999**, *82*, 797–818.
- (23) Long, X.; Ye, Z.-G. New Dielectric and Ferroelectric Solid Solution of (1-x)Ba(Mg_{1/3}Nb_{2/3})O_{3-x}PbTiO₃ with Morphotropic Phase Boundary. *Chem. Mater.* **2007**, *19*, 1285–1289.
- (24) Park, B. H.; Kang, B. S.; Bu, S. D.; Noh, T. W.; Lee, J.; Jo, W. Lanthanum-substituted bismuth titanate for use in non-volatile memories. *Nature* **1999**, *401*, 682–684.
- (25) Ramesh, R.; Lee, J.; Sands, T.; Keramidas, V. G.; Auciello, O. Oriented ferroelectric La-Sr-Co-O/Pb-La-Zr-Ti-O/La-Sr-Co-O heterostructures on [001] Pt/SiO₂ Si substrates using a bismuth titanate template layer. *Appl. Phys. Lett.* **1994**, *64*, 2511–2513.
- (26) Saito, Y.; Takao, H.; Tani, T.; Nonoyama, T.; Takatori, K.; Homma, T.; Nagaya, T.; Nakamura, M. Lead-free piezoceramics. *Nature* **2004**, *432*, 84–87.
- (27) Zylberberg, J.; Belik, A. A.; Takayama-Muromachi, E.; Ye, Z.-G. Bismuth aluminate: A new high-T_C lead-free piezo-/ferroelectric. *Chem. Mater.* **2007**, *19*, 6385–6390.
- (28) Ye, H.-Y.; Zhang, Y.; Fu, D.-W.; Xiong, R.-G. A Displacive-Type Metal Crown Ether Ferroelectric Compound: Ca(NO₃)₂(15-crown-5). *Angew. Chem., Int. Ed.* **2014**, *53*, 6724–6729.
- (29) Fu, D.-W.; Zhang, W.; Cai, H.-L.; Ge, J.-Z.; Zhang, Y.; Xiong, R.-G. Diisopropylammonium chloride: a ferroelectric organic salt with a high phase transition temperature and practical utilization level of spontaneous polarization. *Adv. Mater.* **2011**, *23*, 5658–5662.
- (30) Fu, D.-W.; Cai, H.-L.; Liu, Y.; Ye, Q.; Zhang, W.; Zhang, Y.; Chen, X.-Y.; Giovannetti, G.; Capone, M.; Li, J.; Xiong, R.-G. Diisopropylammonium bromide is a high-temperature molecular ferroelectric crystal. *Science* **2013**, *339*, 425–428.
- (31) Horiuchi, S.; Ishii, F.; Kumai, R.; Okimoto, Y.; Tachibana, H.; Nagaosa, N.; Tokura, Y. Ferroelectricity near room temperature in co-crystals of nonpolar organic molecules. *Nat. Mater.* **2005**, *4*, 163–166.
- (32) Horiuchi, S.; Kumai, R.; Tokura, Y. Hydrogen-bonded donor–acceptor compounds for organic ferroelectric materials. *Chem. Commun.* **2007**, 2321–2329.
- (33) Horiuchi, S.; Tokunaga, Y.; Giovannetti, G.; Picozzi, S.; Itoh, H.; Shimano, R.; Kumai, R.; Tokura, Y. Above-room-temperature ferroelectricity in a single-component molecular crystal. *Nature* **2010**, *463*, 789–792.
- (34) Horiuchi, S.; Tokura, Y. Organic ferroelectrics. *Nat. Mater.* **2008**, *7*, 357–366.
- (35) Jain, P.; Dalal, N. S.; Toby, B. H.; Kroto, H. W.; Cheetham, A. K. Order-Disorder Antiferroelectric Phase Transition in a Hybrid Inorganic-Organic Framework with the Perovskite Architecture. *J. Am. Chem. Soc.* **2008**, *130*, 10450–10451.
- (36) Tayi, A. S.; Shveyd, A. K.; Sue, A. C.-H.; Szarko, J. M.; Rolczynski, B. S.; Cao, D.; Kennedy, T. J.; Sarjeant, A. A.; Stern, C. L.; Paxton, W. F.; Wu, W.; Dey, S. K.; Fahrenbach, A. C.; Guest, J. R.; Mohseni, H.; Chen, L. X.; Wang, K. L.; Stoddart, J. F.; Stupp, S. I. Room-temperature ferroelectricity in supramolecular networks of charge-transfer complexes. *Nature* **2012**, *488*, 485–489.
- (37) Xu, G.-C.; Ma, X.-M.; Zhang, L.; Wang, Z.-M.; Gao, S. Disorder-Order Ferroelectric Transition in the Metal Formate Framework of [NH₄][Zn(HCOO)₃]. *J. Am. Chem. Soc.* **2010**, *132*, 9588–9590.
- (38) Ye, H.-Y.; Fu, D.-W.; Zhang, Y.; Zhang, W.; Xiong, R.-G.; Huang, S. D. Hydrogen-bonded ferroelectrics based on metal-organic coordination. *J. Am. Chem. Soc.* **2009**, *131*, 42–43.
- (39) Ye, Q.; Song, Y.-M.; Wang, G.-X.; Chen, K.; Fu, D.-W.; Hong Chan, P. W.; Zhu, J.-S.; Huang, S. D.; Xiong, R.-G. Ferroelectric metal-

- organic framework with a high dielectric constant. *J. Am. Chem. Soc.* **2006**, *128*, 6554–6555.
- (40) Zhao, H.; Qu, Z.-R.; Ye, H.-Y.; Xiong, R.-G. In situ hydrothermal synthesis of tetrazole coordination polymers with interesting physical properties. *Chem. Soc. Rev.* **2008**, *37*, 84–100.
- (41) Zhao, H.-X.; Zhuang, G.-L.; Wu, S.-T.; Long, L.-S.; Guo, H.-Y.; Ye, Z.-G.; Huang, R.-B.; Zheng, L.-S. Experimental and theoretical demonstration of ferroelectric anisotropy in a one-dimensional copper (II)-based coordination polymer. *Chem. Commun.* **2009**, 1644–1646.
- (42) Zhang, Y.; Ye, H.-Y.; Cai, H.-L.; Fu, D.-W.; Ye, Q.; Zhang, W.; Zhou, Q.; Wang, J.; Yuan, G.-L.; Xiong, R.-G. Switchable Dielectric, Piezoelectric, and Second-Harmonic Generation Bistability in a New Improper Ferroelectric above Room Temperature. *Adv. Mater.* **2014**, *26*, 4515–4520.
- (43) Cui, H.; Wang, Z.; Takahashi, K.; Okano, Y.; Kobayashi, H.; Kobayashi, A. Ferroelectric porous molecular crystal, $[\text{Mn}_3(\text{HCOO})_6](\text{C}_2\text{H}_5\text{OH})$, exhibiting ferrimagnetic transition. *J. Am. Chem. Soc.* **2006**, *128*, 15074–15075.
- (44) Di Sante, D.; Stroppa, A.; Jain, P.; Picozzi, S. Tuning the Ferroelectric Polarization in a Multiferroic Metal-Organic Framework. *J. Am. Chem. Soc.* **2013**, *135*, 18126–18130.
- (45) Jain, P.; Ramachandran, V.; Clark, R. J.; Zhou, H. D.; Toby, B. H.; Dalal, N. S.; Kroto, H. W.; Cheetham, A. K. Multiferroic Behavior Associated with an Order-Disorder Hydrogen Bonding Transition in Metal–Organic Frameworks (MOFs) with the Perovskite ABX_3 Architecture. *J. Am. Chem. Soc.* **2009**, *131*, 13625–13627.
- (46) Ohkoshi, S.-i.; Tokoro, H.; Matsuda, T.; Takahashi, H.; Irie, H.; Hashimoto, K. Coexistence of ferroelectricity and ferromagnetism in a rubidium manganese hexacyanoferrate. *Angew. Chem., Int. Ed.* **2007**, *46*, 3238–3241.
- (47) Rogez, G.; Viart, N.; Drillon, M. Multiferroic materials: the attractive approach of metal-organic frameworks (MOFs). *Angew. Chem., Int. Ed.* **2010**, *49*, 1921–1923.
- (48) Stroppa, A.; Barone, P.; Jain, P.; Perez-Mato, J. M.; Picozzi, S. Hybrid Improper Ferroelectricity in a Multiferroic and Magneto-electric Metal-Organic Framework. *Adv. Mater.* **2013**, *25*, 2284–2290.
- (49) Stroppa, A.; Jain, P.; Barone, P.; Marsman, M.; Perez-Mato, J. M.; Cheetham, A. K.; Kroto, H. W.; Picozzi, S. Electric control of magnetization and interplay between orbital ordering and ferroelectricity in a multiferroic metal–organic framework. *Angew. Chem., Int. Ed.* **2011**, *50*, 5847–5850.
- (50) Thomson, R. I.; Jain, P.; Cheetham, A. K.; Carpenter, M. A. Elastic relaxation behavior, magnetoelastic coupling, and order-disorder processes in multiferroic metal-organic frameworks. *Phys. Rev. B: Condens. Matter Mater. Phys.* **2012**, *86*, 214304.
- (51) Hang, T.; Zhang, W.; Ye, H.-Y.; Xiong, R.-G. Metal-organic complex ferroelectrics. *Chem. Soc. Rev.* **2011**, *40*, 3577–3598.
- (52) Zhang, Y.; Ye, H.-Y.; Fu, D.-W.; Xiong, R.-G. An Order-Disorder Ferroelectric Host-Guest Inclusion Compound. *Angew. Chem., Int. Ed.* **2014**, *53*, 2114–2118.
- (53) Zhang, W.; Xiong, R.-G. Ferroelectric metal-organic frameworks. *Chem. Rev.* **2012**, *112*, 1163–1195.
- (54) Zhang, W.; Ye, H.-Y.; Xiong, R.-G. Metal-organic coordination compounds for potential ferroelectrics. *Coord. Chem. Rev.* **2009**, *293*, 2980–2997.
- (55) Srivastava, A. K.; Praveenkumar, B.; Mahawar, I. K.; Divya, P.; Shalini, S.; Boomishankar, R. Anion Driven $[\text{Cu}^{\text{II}}\text{L}_2]_n$ Frameworks: Crystal Structures, Guest-Encapsulation, Dielectric, and Possible Ferroelectric Properties. *Chem. Mater.* **2014**, *26*, 3811–3817.
- (56) Sheldrick, G. M. A short history of SHELX. *Acta Crystallogr., Sect. A: Found. Crystallogr.* **2008**, *64*, 112–122.
- (57) Blatov, V. A.; Shevchenko, A. P.; Proserpio, D. M. Applied Topological Analysis of Crystal Structures with the Program Package ToposPro. *Cryst. Growth Des.* **2014**, *14*, 3576–3586.
- (58) Blatov, V. A.; Shevchenko, A. P.; Serezhkin, V. N. TOPOS3.2: A new version of the program package for multipurpose crystal-chemical analysis. *J. Appl. Crystallogr.* **2000**, *33*, 1193–1193.
- (59) O’Keeffe, M.; Yaghi, O. M. Deconstructing the crystal structures of metal-organic frameworks and related materials into their underlying nets. *Chem. Rev.* **2012**, *112*, 675–702.
- (60) Thirumurugan, A.; Li, W.; Cheetham, A. K. Bismuth 2,6-pyridinedicarboxylates: assembly of molecular units into coordination polymers, CO_2 sorption and photoluminescence. *Dalton Trans.* **2012**, *41*, 4126–4134.
- (61) Ok, K. M.; Chi, E. O.; Halasyamani, P. S. Bulk characterization methods for non-centrosymmetric materials: second-harmonic generation, piezoelectricity, pyroelectricity, and ferroelectricity. *Chem. Soc. Rev.* **2006**, *35*, 710–717.
- (62) Li, Y.-H.; Qu, Z.-R.; Zhao, H.; Ye, Q.; Xing, L.-X.; Wang, X.-S.; Xiong, R.-G.; You, X.-Z. A novel TGS-like inorganic-organic hybrid and a preliminary investigation of its possible ferroelectric behavior. *Inorg. Chem.* **2004**, *43*, 3768–3770.
- (63) Law, C. W.; Tong, K. Y.; Li, J. H.; Li, K. Leakage current in PZT films with sputtered RuO_x electrodes. *Solid-State Electron.* **2000**, *44*, 1569–1571.
- (64) Menzl, G.; Köfinger, J.; Dellago, C. Phase transition and interporc correlations of water in nanopore membranes. *Phys. Rev. Lett.* **2012**, *109*, 020602.
- (65) Luo, C.-F.; Fa, W.; Zhou, J.; Dong, J.-M.; Zeng, X.-C. Ferroelectric ordering in ice nanotubes confined in carbon nanotubes. *Nano Lett.* **2008**, *8*, 2607–2612.
- (66) Dong, X.-Y.; Li, B.; Ma, B.-B.; Li, S.-J.; Dong, M.-M.; Zhu, Y.-Y.; Zang, S.-Q.; Song, Y.; Hou, H.-W.; Mak, T. C. W. Ferroelectric switchable behavior through fast reversible de/adsorption of water spirals in a chiral 3D metal-organic framework. *J. Am. Chem. Soc.* **2013**, *135*, 10214–10217.
- (67) Compounds having dielectric constant value greater than that of silicon nitride ($\epsilon_r > 7.0$) are classified as high dielectric constant materials.
- (68) The TGA and DSC profile of **1**_{desolvated} shows no weight loss until 270 °C. However, the TGA and DSC graphs of **1**_{resolvated} closely resembles to that of **1**.
- (69) Jin, L.; Li, F.; Zhang, S. Decoding the fingerprint of ferroelectric loops: comprehension of the material properties and structures. *J. Am. Ceram. Soc.* **2014**, *97*, 1–27.
- (70) Chen, J.L.; Chen, H.m.; Lee, J. Y. An investigation on the leakage current and time dependent dielectric breakdown of ferroelectric lead-zirconate-titanate thin film capacitors for memory device applications. *Appl. Phys. Lett.* **1996**, *69*, 4011–4013.
- (71) Yang, J.-K.; Kim, W. S.; Park, H.-H. Effect of grain size of $\text{Pb}(\text{Zr}_{0.4}\text{Ti}_{0.6})\text{O}_3$ sol-gel derived thin films on the ferroelectric properties. *Appl. Surf. Sci.* **2001**, *169-170*, 544–548.
- (72) Cui, H.; Zhou, B.; Long, L.-S.; Okano, Y.; Kobayashi, H.; Kobayashi, A. A Porous Coordination-Polymer Crystal Containing One-Dimensional Water Chains Exhibits Guest-Induced Lattice Distortion and a Dielectric Anomaly. *Angew. Chem., Int. Ed.* **2008**, *47*, 3376–3380.
- (73) Cui, H.-B.; Takahashi, K.; Okano, Y.; Kobayashi, H.; Wang, Z.; Kobayashi, A. Dielectric properties of porous molecular crystals that contain polar molecules. *Angew. Chem., Int. Ed.* **2005**, *44*, 6508–6512.
- (74) Wang, Z. M.; Hu, K.; Gao, S.; Kobayashi, H. Formate-Based Magnetic Metal-Organic Frameworks Templated by Protonated Amines. *Adv. Mater.* **2010**, *22*, 1526–1533.